Magnetic Behavior of Li-Doped and Pure MnTe: A Muon Spin Relaxation Analysis

Camille Shaw

A senior thesis submitted to the faculty of
Brigham Young University
in partial fulfillment of the requirements for the degree of

Bachelor of Science

Benjamin Frandsen, Advisor

Department of Physics and Astronomy

Brigham Young University

ABSTRACT

Magnetic Behavior of Li-Doped and Pure MnTe: A Muon Spin Relaxation Analysis

Camille Shaw
Department of Physics and Astronomy, BYU
Bachelor of Science

We report a detailed muon spin relaxation/rotation (μSR) investigation of the multifunctional antiferromagnet MnTe, including samples of pure MnTe and samples doped with small amounts of Li. The μSR shows unusually complex behavior as a function of temperature: Upon cooling from T_N = 307 K to 2 K, we observe the appearance, subsequent disappearance, and ultimate reappearance of up to four distinct muon precession frequency branches. In addition, for intermediate temperatures between approximately 40 K and 100 K, we observe a nearly instantaneous depolarization of the muon spin ensemble, resulting in the complete loss of the , which is then recovered upon further cooling or warming. We performed muon stopping site calculations using density functional theory to gain a better understanding of the μSR data, identifying two crystallographically distinct sets of that are nearly degenerate in the energy of the muon-lattice system. The observed muon precession frequencies can be qualitatively accounted for by these and the antiferromagnetic domain structure of pure and doped MnTe. We argue that the unusual loss and recovery of the oscillations at intermediate temperatures is a consequence of thermally assisted muon hopping between the nearly degenerate . The results provide useful information about MnTe itself and highlight the possibility of rich muon dynamics in non-oxide magnetic semiconductors.

Keywords: Muon spin relaxation, Magnetic systems, Magnetic phase transitions

ACKNOWLEDGMENTS

I thank the scientific staff at TRIUMF for their valuable assistance during the experiments. This work was supported by the U.S. Department of Energy, Office of Science, Basic Energy Sciences (DOE-BES) through Award No. DE-SC0021134. I thank Brigham Young University for their support in creating undergraduate research opportunities. I thank my research advisor Dr. Benjamin Frandsen for his guidance during this research project.

Contents

Table of Contents **iv**

List of Figures **v**

1 Introduction **1**
1.1 Magnetic Properties 1
1.2 Structure 1
1.3 Motivation 3
1.4 Experiment 4

2 Methods **5**
2.1 Sample synthesis and bulk characterization 5
2.2 Muon spin relaxation/rotation 5
2.3 Muon Site Determination 7

3 Results **9**
3.1 Zero-Field μSR Data 9
3.2 DFT Results 13

4 Discussion **15**
4.1 Future Work 16

Bibliography **17**

Index **20**

List of Figures

1.1 Crystal and magnetic structure of MnTe. Purple and gold spheres represent the Mn and Te atoms, respectively; the gray spheres mark the expected position of Li dopants for Li MnTe. The arrows represent the magnetic moments in the magnetic ground state of pure MnTe; for Li MnTe, the spin direction rotates to point primarily along c. The green and red spheres show the two crystallographically distinct muon that minimize the energy as calculated by DFT. 2

3.1 Least squares regression analysis of the long-time μSR data for the Li variants of MnTe. Each panel has three representative temperatures: low, medium, and high, which illustrate the change in relaxation rate. 9

3.2 Least squares regression analysis of the short-time μSR data for the Li variants of MnTe. Each panel has three representative temperatures: low, intermediate, and high, which exhibit different oscillation frequencies. 10

3.3 Time-integrated ZF as a function of temperature for the pure and Li samples of MnTe. The integrated is lost in the 40-90K temperature range for the pure sample. However, as Li doping increases, the disappearance becomes less pronounced and shifts to the 70-120K temperature range. 11

3.4 Frequencies w_1 and w_2 obtained from short-time fits for 0.5% and 5% Li MnTe samples, plotted as a function of temperature. 13

Chapter 1

Introduction

1.1 Magnetic Properties

The antiferromagnetic semiconductor MnTe has recently emerged as an exciting material in several different areas of fundamental and applied interest in condensed matter and materials physics. Among other exceptional attributes, MnTe is a high-performance thermoelectric material when lightly [1–5]; a viable candidate for antiferromagnetic-based spintronic devices [6]; the magnetic component of the intrinsic magnetic topological insulator $MnBi_2Te_4$ [7]; a magnetostructurally active material with the largest known spontaneous magnetovolume effect in an antiferromagnet [8]; and a prototypical example of the subset of spin-splitting antiferromagnets [9, 10] often called altermagnets [11–13], which are characterized by fully compensated spin sublattices for which the specific combination of symmetries present can lift the spin degeneracy of the electronic bands.

1.2 Structure

MnTe possesses the hexagonal NiAs structure (space group $P6_3/mmc$), in which the Mn and Te atoms all sit on high-symmetry sites (Fig. 1.1). When with charge carriers such as Na and Li, the

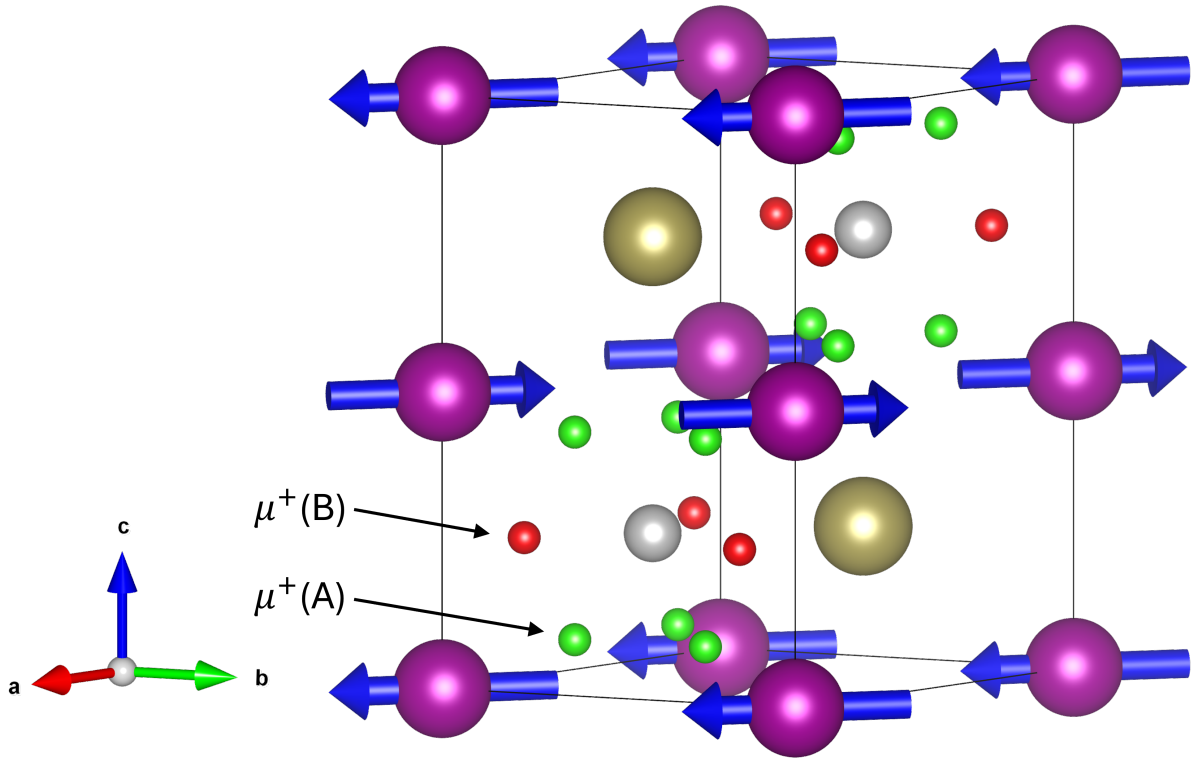

Figure 1.1 Crystal and magnetic structure of MnTe. Purple and gold spheres represent the Mn and Te atoms, respectively; the gray spheres mark the expected position of Li dopants for Li MnTe. The arrows represent the magnetic moments in the magnetic ground state of pure MnTe; for Li MnTe, the spin direction rotates to point primarily along c. The green and red spheres show the two crystallographically distinct muon that minimize the energy as calculated by DFT.

dopant atoms are thought to occupy interstitial sites above and below the Te atoms along the *c* axis [14], as illustrated in Fig. 1.1. The $S = 5/2$ spins localized on the Mn atoms transition to a long-range-ordered antiferromagnetic configuration below the Nèel temperature $T_N = 307$ K, in which spins within a common *ab* plane are aligned within the plane, but the spin direction reverses between subsequent planes of Mn atoms while moving along the *c* axis [15, 16]. Interestingly, even for minute levels of Li doping as low as 0.3%, the spin direction rotates to be nearly aligned with the *c* axis at low temperature, only to reorient back into the *ab* plane abruptly when warming toward T_N [14]. This behavior points to delicately balanced competing magnetic ground states in MnTe and hints at the possibility of controllable switching between these distinct spin orientations. Also of note is the robust persistence of dynamically correlated short-range (sub-nanometer) antiferromagnetic correlations far into the nominally paramagnetic phase above T_N [17], which have been shown to play a decisive role in both the high-performance thermoelectric properties [18] and the large magnetovolume effect [8].

1.3 Motivation

Considering the central importance of the magnetism to nearly all of the notable properties and potential applications of MnTe, there is a continued need to utilize advanced magnetic probes to study MnTe and develop a complete picture of its magnetic properties, including both the magnetic structure and dynamics. To that end, muon spin relaxation/rotation (μSR) is particularly attractive studying MnTe. This technique [19], which entails implanting spin-polarized positive muons in the sample and observing the asymmetric decay of the muons into positrons, is sensitive to both long-range and short-range spin configurations, can reliably measure the volume fraction of competing magnetic phases, and probes spin dynamics on a slower time scale than inelastic neutron scattering

but faster than conventional magnetometry techniques, making it highly complementary to these other methods.

1.4 Experiment

Here, we report extensive μSR experiments on samples of pure MnTe and Li-doped MnTe with Li concentrations of 0.5%, 2%, and 5%, greatly expanding upon the initial μSR results on MnTe recently published [20]. We reveal a complex temperature dependence of the zero-field μSR in pure MnTe, including the emergence of multiple muon precession frequencies at temperatures just below T_N, followed by the disappearance of the oscillations and an anomalous damping of the long-time μSR at intermediate temperatures, and ultimately a recovery of the oscillations at the lowest temperatures. These unusual features of the μSR data can be modified systematically with Li doping. With the aid of muon stopping site calculations using density functional theory, we qualitatively account for the observed oscillation frequencies based on the predicted and the AFM domain structure of MnTe, and we propose an explanation for the observed damping of the long-time and disappearance of the oscillations based on thermally assisted muon hopping among nearly-degenerate in the lattice. This work not only fills in a gap in the experimental literature on MnTe by providing detailed μSR results for this system, but also contributes to the ongoing effort to gain a deeper understanding of how implanted muons both affect and are affected by the host lattice in quantum materials.

Chapter 2

Methods

2.1 Sample synthesis and bulk characterization

The sample of pure MnTe used in this study is the same one used in Ref. [14], and the samples of Li- MnTe were prepared in identical fashion as in Ref. [14]; we refer the reader to Ref. [14] for full details regarding the synthesis and bulk characterization. Briefly, the pure MnTe was synthesized via solid-state reaction in an evacuated silica ampoule, and the samples were synthesized via ball milling and hot pressing. Rietveld refinement of x-ray diffraction data confirmed the expected hexagonal structure for all samples, with small impurity phases (3 wt. % or less) of $MnTe_2$ in the pure sample and MnO in the samples. These small impurities have a negligible effect on the μSR data, since μSR is a local probe such that the signal from these impurity phases is proportional to their volume fraction in the sample, which is of order 1%.

2.2 Muon spin relaxation/rotation

Muon spin relaxation/rotation (μSR) is an experimental technique used to probe the magnetic properties of materials. In this technique spin-polarized, positively charged muons are implanted

into the sample, where they come to rest at interstitial sites that correspond to local minima in the total energy. The muon spin precesses in the local magnetic field at its location, where the local field is the vector sum of any externally applied field and the internal magnetic field caused by electronic spins and/or nuclear dipolar moments. The muon decays into a positron and two neutrinos shortly after entering the material, with a mean lifetime of 2.2 μs. Crucially, the positron is emitted preferentially in the direction of the parent muon's spin at the moment of decay. Detectors surrounding the material measure the distribution of emitted positrons as a function of time after muon implantation, yielding information about the temporal evolution of the muon spins and thus the local magnetic field distribution. Specifically, the time-dependent is calculated for a pair of detectors placed on opposite sides of the sample as

$$a(t) = \frac{N_1(t) - N_2(t)}{N_1(t) + N_2(t),} \tag{2.1}$$

where N_1 and N_2 are the numbers of positron events recorded by the two detectors [21]. This quantity is proportional to the projection of the average muon spin polarization onto the direction defined by the axis joining the two detectors.

We performed μSR experiments on the M20D beamline at TRIUMF Laboratory in Vancouver, Canada. Two sample environments were used: a helium gas flow cryostat providing access to temperatures between 2 K and 300 K, and a Thermo Haake Phoenix P1 water circulator for temperatures between 243 K and 573 K. For pure MnTe, we collected data over a temperature range of 2 K to 450 K. For the Li variants, the data span the temperature range 2 K to 300 K. We collected data in three magnetic field conditions: zero field (ZF); longitudinal field (LF), in which a magnetic field with strength up to 0.4 T was applied parallel to the initial muon spin direction; and weak transverse field (wTF), in which a small field in the range 0.003 – 0.005 T was applied perpendicular to the initial muon spin direction. We collected 10 to 15 million positron events for ZF runs, 3 to 5 million for wTF runs, and 8 to 10 million for LF runs.

We analyzed the μSR data collected at TRIUMF using the open-source python program BEAMS [22], which performs least-squares optimization to fit user-defined mathematical functions to the data. The program can also be used to compute the time-integrated . The parameter α is a geometric constant that accounts for experimental asymmetries arising from the relative positioning of the detectors. Specifically, if one detector is positioned closer to the sample, it subtends a larger solid angle, thereby detecting a greater number of positron events as an experimental artifact. The value of α was determined either through weak transverse field (wTF) measurements at temperatures above T_N when accessible, or alternatively, from the long-time baseline of fast-relaxing zero-field (ZF) spectra when such temperatures could not be reached.

2.3 Muon Site Determination

To aid in the interpretation of the μSR data, we used the program Mufinder [23] to computationally model the muon in MnTe. Mufinder uses density functional theory as implemented in CASTEP to insert positively charged muons into the MnTe unit cell at several randomly generated positions, relax the structure for each candidate muon site, and then calculate the total energy to find the most energetically favorable muon . Then, using the model of the relaxed structure with the implanted muon, the internal magnetic field at the muon site is calculated based on the known long-range magnetic structure. This allows for a direct comparison with the ZF μSR data.

We carried out density functional theory (DFT) calculations using the plane-wave basis-set electronic structure code CASTEP. Calculations were carried out within the generalized-gradient approximation (GGA) using the PBE functional. A collinear treatment of the spin was used, with an antiferromagnetic arrangement of the two Mn atoms within the unit cell, and the system was treated as non-spin-polarized. Below 14K, MnTe crystallizes in the hexagonal $P63/mmc$ space group, with $a = 4.1273\,\text{Å}$ and $c = 6.6589\,\text{Å}$.

Structural relaxations with the muon were carried out on a supercell comprising $3 \times 3 \times 2$ conventional unit cells of MnTe to reduce the unphysical interaction of the muon with its periodic images. For these calculations, we used a smaller $2 \times 2 \times 2$ Monkhorst-Pack grid for Brillouin zone sampling, reflecting the larger size of the supercell when compared to the unit cell. Muon site calculations were carried out using the MuFinder program [23].

Initial structures comprising a muon and the MnTe supercell were generated by requiring the muon to be at least 0.5 Å away from each of the muons in the previously generated structures (including their symmetry equivalent positions) and at least 1.0 Å away from any of the atoms in the cell. This resulted in 28 structures which were subsequently allowed to relax until the calculated forces on the atoms were all $< 5 \times 10^{-2}\,\mathrm{eV\,\AA^{-1}}$ and the total energy and atomic positions converged to within 2×10^{-5} eV per atom and 1×10^{-3} Å, respectively.

Chapter 3

Results

3.1 Zero-Field μSR Data

Fig. 3.1 shows the μSR data on a long time scale. The fastest relaxation occurs in the intermediate

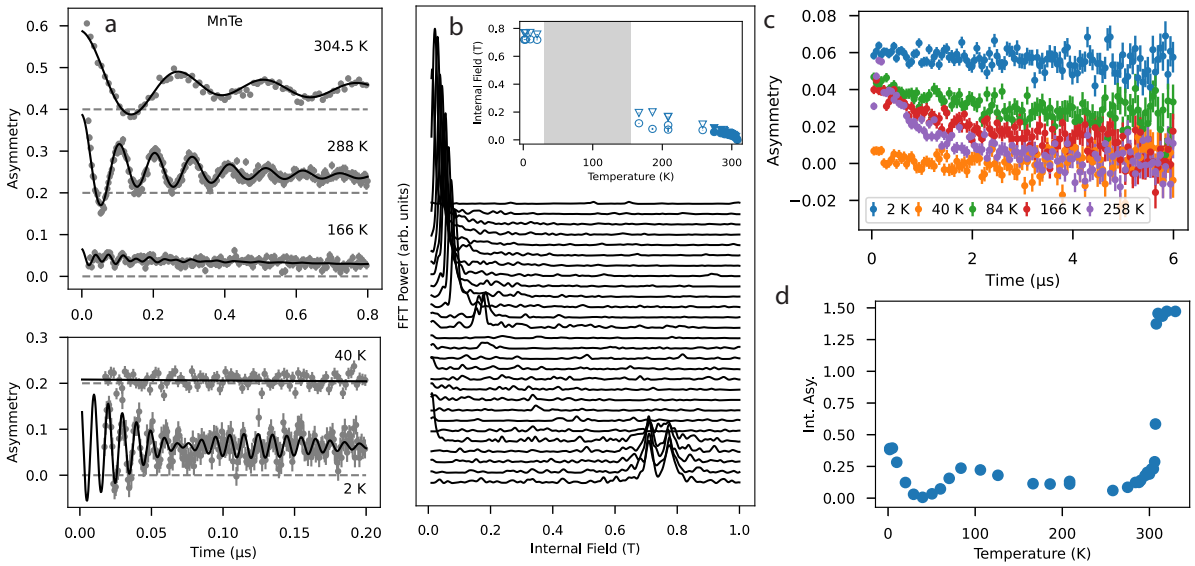

Figure 3.1 Least squares regression analysis of the long-time μSR data for the Li variants of MnTe. Each panel has three representative temperatures: low, medium, and high, which illustrate the change in relaxation rate.

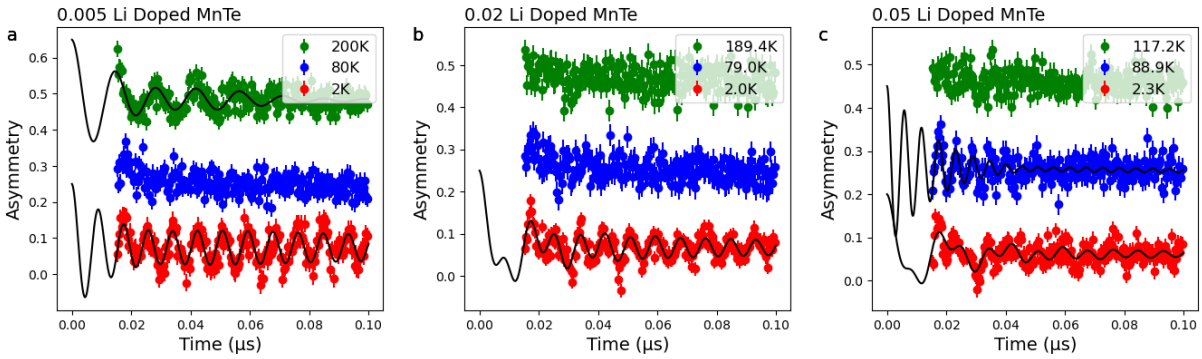

Figure 3.2 Least squares regression analysis of the short-time μSR data for the Li variants of MnTe. Each panel has three representative temperatures: low, intermediate, and high, which exhibit different oscillation frequencies.

temperature range of 80-90K. In contrast, the slowest relaxation is observed at low temperatures around 2K. High temperatures between 120K and 200K show relaxation rates between the middle and low temperature ranges. Below the the μSR signal exhibits two distinct components. The first is a 2/3 component showing oscillations, which arises from muons precessing around local magnetic moments. The second is a 1/3 component displaying relaxation, occurring when muon spins align parallel or anti-parallel to the local magnetic field, eliminating precession due to the absence of torque. This behavior is characteristic of μSR in materials with static internal magnetic fields, providing insights into the magnetic order of MnTe below its critical temperature. The long-time behavior, as depicted in Fig. 3.1, results from time binning that effectively averages out the oscillations. This averaging process reveals the underlying relaxation trends across different temperatures. Once the material crosses the , it becomes paramagnetically aligned, thus eliminating this effect.

The long time is modeled with a stretched exponential in the form:

$$a(t) = a_0 e^{-(\lambda t)^{\beta}}. \tag{3.1}$$

We display the integrated zero-field for all four samples in Fig. 3.3.

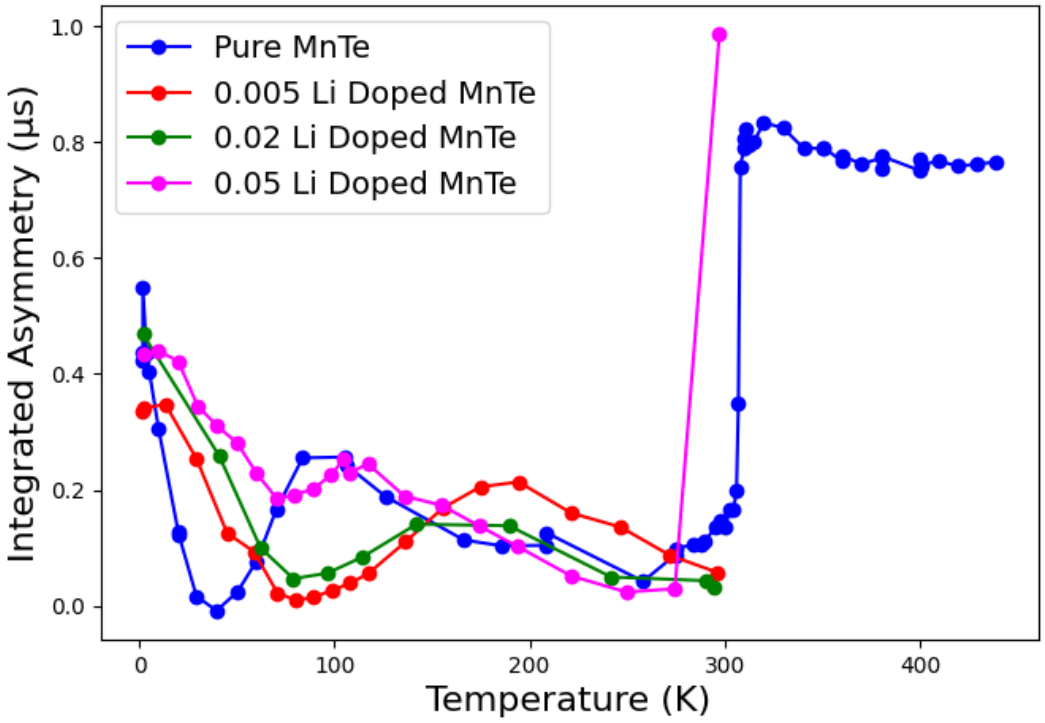

Figure 3.3 Time-integrated ZF as a function of temperature for the pure and Li samples of MnTe. The integrated is lost in the 40-90K temperature range for the pure sample. However, as Li doping increases, the disappearance becomes less pronounced and shifts to the 70-120K temperature range.

At low temperatures, the integrated exhibits a high value; however, it decreases progressively with increasing temperature, eventually approaching zero. Interestingly, a recovery of is observed within the 40˜90K range for the pure and 5% samples, and within the 110˜220K range for the 0.5% and 0.2% Li doped samples. Following this recovery, the again diminishes toward zero before sharply increasing at the as the system transitions into the paramagnetic state.

Fig. 3.2 illustrates the short-time behavior of the μSR , data. For the 0.5% Li sample, oscillations are observed at both high and low temperatures, but vanish in the intermediate temperature range, consistent with the behavior of the integrated shown in fig. 3.3. In contrast, the 0.2% Li sample

shows oscillations only at low temperatures, while the 0.5% Li sample shows oscillations at low temperatures that are absent at higher temperatures. The disappearance of oscillations beyond a certain temperature is a more common relationship in μSR experiments and is likely attributed to the increased doping concentration introducing magnetic distortions within the material's structure. Additionally, as the Li doping concentration increases, the oscillations become noisier, which can also be attributed to these magnetic distortions disrupting spin coherence.

A damped cosine combined with a stretched exponential in the form:

$$A(t) = a_0 e^{-(\lambda t)^{\beta}} + a_1 \sum_{i=1}^{2} C_i \cos(\omega_i t) e^{-\lambda_i t}, \tag{3.2}$$

The frequency parameters derived from short-time fits are presented in Fig. 3.4. For the 0.5% sample, the frequencies show a linear decrease with temperature, except within the anomalous temperature range of 40–90K. This behavior suggests that, in the absence of loss within this range, the frequency would continue to decrease linearly with temperature. Such a trend is expected, as at low temperatures, atomic positions are more rigid, leading to greater uniformity among their spins. As the temperature increases, the additional thermal energy allows spins to rearrange more readily, disrupting this uniformity. With increasing Li doping concentration, the frequencies remain relatively constant until temperatures associated with loss are approached, as shown in the 0.5% panel of Fig. 3.4. This behavior can be attributed to the introduction of structural randomness caused by higher dopant concentrations, which disrupts the material's magnetic properties and reduces the coherence of spin interactions.

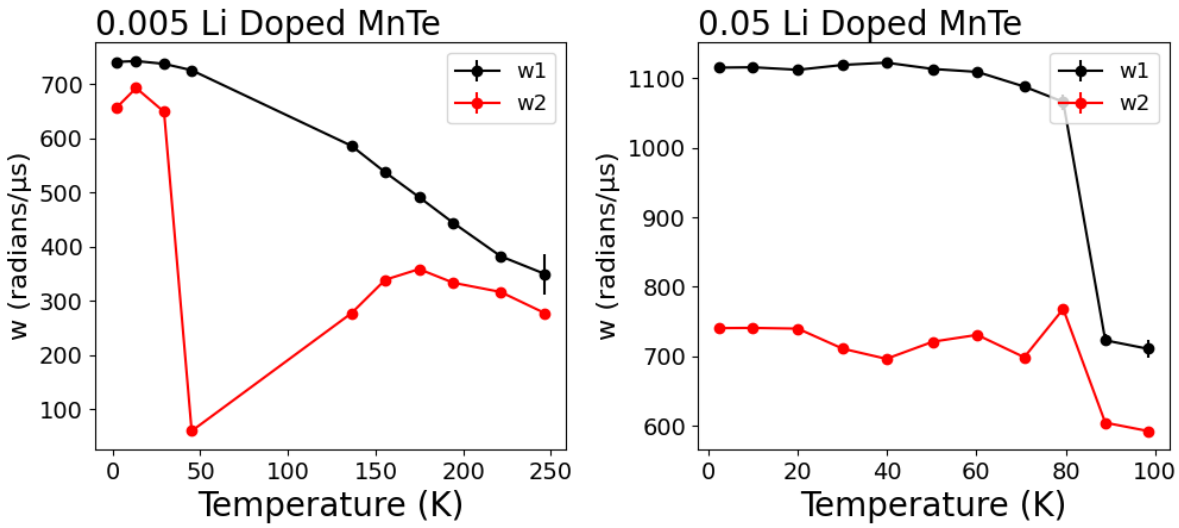

Figure 3.4 Frequencies w_1 and w_2 obtained from short-time fits for 0.5% and 5% Li MnTe samples, plotted as a function of temperature.

3.2 DFT Results

From these structural relaxations, we identified two crystallographically distinct muon . These sites are shown within the unit cell of MnTe in Fig. 1.1. At site A, the muon sits 1.56Å from an Mn atom. This Mn atom is pulled 0.025Å towards the muon with all of the muon-induced distortions being quite small in this case, i.e., below 0.1Å. We also find a second distinct site, site B, 0.066 eV higher in energy than site A, in which the muon sits 1.84Å from a Te atom. The nearest Te atom is pushed 0.39Å away from the muon site. The muon-induced distortions are significantly larger for site B than they are for site A. However, the energies of these sites are comparable, so we cannot rule out either of them on energetic grounds.

We note that the sites obtained from the structural relaxation approach are distinct from the one proposed on the basis on the minimum of the electrostatic potential. That site is unstable when allowing the structure to relax. A muon starting about this position moves along the c axis from

$z = 0.169$ to $z = 0.06$. Furthermore, the relaxed muon site is 0.54 eV higher in energy than the lowest energy muon site obtained from structural relaxations. We therefore concluded that there are likely to be two candidate muon , that are approximately equally likely to be occupied.

Chapter 4

Discussion

In Fig. 3.3, all variations of MnTe exhibited high at low temperatures, indicating the presence o.f a homogeneous magnetic field. The μSR experiment results revealed a static and relatively uniform magnetic field distribution arising from the magnetic moments throughout MnTe at low temperatures. However, with increasing doping concentration, the oscillations became noisier, suggesting a broader distribution of magnetic field strengths at the muon sites, likely due to distortions introduced by the dopant atoms. As expected, we observed a spike in the as the material crossed the , signifying the transition to a paramagnetic state.

Several hypotheses may explain the disappearance of in the 40-90 K range. Fig. 1.1 indicates the presence of two energetically homogeneous for implanted muons. Although energetically equivalent, these sites likely possess different local magnetic structures. The existence of two stopping locations may contribute to the two frequencies observed in the oscillations of the short-time data in Fig. 3.2. Muon hopping between these sites with distinct local magnetic environments could alter the oscillation frequency, resulting in multi-frequency behavior. This phenomenon may also contribute to the loss of in the intermediate temperature range, as an increasing number of frequencies could lead to mutual dampening, reducing the signal to noise. Additionally, unpublished mpdf data reveals shifting of Te atoms within this temperature range. The temperature dependence

of Te atom distortions could indicate that hopping is favored in this temperature regime, potentially explaining the anomalous behavior. As a charged particle, the muon exerts its own magnetic field, potentially disturbing the magnetic structure of MnTe. The muon may play a role similar to a positive Li^+ dopant ion, possibly triggering spin reorientation in its local environment, mirroring the global behavior observed in Li- samples.

4.1 Future Work

It remains challenging to definitively conclude whether this behavior is an intrinsic feature of MnTe related to poorly understood spin fluctuations or an artifact of the experimental method arising from muon-material interactions. Further investigations of MnTe and its Li variants within this temperature regime are necessary. Neutron spin echo experiments could potentially reveal spin relationships not captured by neutron diffraction, as neutrons provide a higher-energy probe compared to muons.

Bibliography

[1] Y. Xu, W. Li, C. Wang, J. Li, Z. Chen, S. Lin, Y. Chen, and Y. Pei, "Performance optimization and single parabolic band behavior of thermoelectric MnTe," J. Mater. Chem. A **5,** 19143–19150 (2017).

[2] Y. Ren, J. Yang, Q. Jiang, D. Zhang, Z. Zhou, X. Li, J. Xin, and X. He, "Synergistic effect by Na doping and S substitution for high thermoelectric performance of p-type MnTe," J. Mater. Chem. C **5,** 5076–5082 (2017).

[3] W. Xiong *et al.*, "Lattice Distortions and Multiple Valence Band Convergence Contributing to High Thermoelectric Performance in MnTe," Small **19,** 2206058 (2023).

[4] S. Zulkifal *et al.*, "Multiple Valence Bands Convergence and Localized Lattice Engineering Lead to Superhigh Thermoelectric Figure of Merit in MnTe," Adv. Sci. p. 2206342 (2023).

[5] S. Zulkifal *et al.*, "All-Scale Hierarchical Structuring, Optimized Carrier Concentration, and Band Manipulation Lead to Ultra-High Thermoelectric Performance in Eco-Friendly MnTe," Small **20,** 2310123 (2024).

[6] D. Kriegner *et al.*, "Multiple-stable anisotropic magnetoresistance memory in antiferromagnetic MnTe," Nat. Commun. **7,** 11623 (2016).

[7] Y. Deng, Y. Yu, M. Z. Shi, Z. Guo, Z. Xu, J. Wang, X. H. Chen, and Y. Zhang, "Quantum anomalous Hall effect in intrinsic magnetic topological insulator $MnBi_2Te_4$," Science **367,** 895–900 (2020).

[8] R. Baral, A. M. Abeykoon, B. J. Campbell, and B. A. Frandsen, "Giant Spontaneous Magnetostriction in MnTe Driven by a Novel Magnetostructural Coupling Mechanism," Adv. Funct. Mater. **33,** 2305247 (2023).

[9] L.-D. Yuan, Z. Wang, J.-W. Luo, E. I. Rashba, and A. Zunger, "Giant momentum-dependent spin splitting in centrosymmetric low-Z antiferromagnets," Phys. Rev. B **102,** 014422 (2020).

[10] L.-D. Yuan, Z. Wang, J.-W. Luo, and A. Zunger, "Prediction of low-Z collinear and noncollinear antiferromagnetic compounds having momentum-dependent spin splitting even without spin-orbit coupling," Phys. Rev. Materials **5,** 014409 (2021).

[11] I. I. Mazin, "Altermagnetism in MnTe: Origin, predicted manifestations, and routes to detwinning," Phys. Rev. B **107,** L100418 (2023).

[12] J. Krempaský *et al.*, "Altermagnetic lifting of Kramers spin degeneracy," Nature **626,** 517–522 (2024).

[13] S. Lee *et al.*, "Broken Kramers Degeneracy in Altermagnetic MnTe," Phys. Rev. Lett. **132,** 036702 (2024).

[14] D. H. Moseley *et al.*, "Giant doping response of magnetic anisotropy in MnTe," Phys. Rev. Materials **6,** 014404 (2022).

[15] N. Kunitomi, Y. Hamaguchi, and S. Anzai, "Neutron diffraction study on manganese telluride," J. Phys.-Paris **25,** 568–574 (1964).

[16] W. Szuszkiewicz, E. Dynowska, B. Witkowska, and B. Hennion, "Spin-wave measurements on hexagonal MnTe NiAs-type structure by inelastic neutron scattering," Phys. Rev. B **73,** 104403 (2006).

[17] R. Baral *et al.*, "Real-space visualization of short-range antiferromagnetic correlations in a magnetically enhanced thermoelectric," Matter **5,** 1853–1864 (2022).

[18] Y. Zheng *et al.*, "Paramagnon drag in high thermoelectric figure of merit Li-doped MnTe," Sci. Adv. **5,** eaat9461 (2019).

[19] A. D. Hillier *et al.*, "Muon spin spectroscopy," Nat. Rev. Methods Primers **2,** 4 (2022).

[20] G. Yumnam *et al.*, "Magnon gap tuning in lithium-doped MnTe," Phys. Rev. B **109,** 214434 (2024).

[21] S. J. Blundell, "Spin-polarized muons in condensed matter physics," Contemporary Physics **40,** 175–192 (2010).

[22] K. A. Petersen, J. Black, and B. A. Frandsen, "BEAMS: Basic and Effective Analysis for Muon spin Spectroscopy," p. https://github.com/FrandsenGroup/beams (2021).

[23] B. Huddart, A. Hernández-Melián, T. Hicken, M. Gomilšek, Z. Hawkhead, S. Clark, F. Pratt, and T. Lancaster, "MuFinder: A program to determine and analyse muon stopping sites," Computer Phys. Comm. **280,** 108488 (2022).

Index

μSR, 5–7

asymmetry, ii, 4, 6, 7, 10–12, 15, 16

doped, 1, 2, 5, 6, 9–13, 16, 20

lithium-, 11

Néel temperature, 10, 11, 15

stopping sites, ii, 2, 4, 7, 13–15